ACS Macro Letters
Cite This: ACS Macro Lett. 2020, 9, 61−69
Letter
pubs.acs.org/macroletters

Self-Assembled Saccharide-Functionalized Amphiphilic Metallacycles as Biofilms Inhibitor via "Sweet Talking"

Guoqing Tao,[†] Tan Ji,[‡] Ning Wang,[§] Guang Yang,[†] Xiaolai Lei,[⊥] Wei Zheng,[‡] Rongying Liu,[†] Xuyang Xu,[†] Ling Yang,[§] Guang-Qiang Yin,[‡,#] Xiaojuan Liao,[○] Xiaopeng Li,[#] Hong-ming Ding,[∥] Xiaoming Ding,[⊥] Jinfu Xu,[*,§] Hai-Bo Yang,[*,‡] and Guosong Chen[*,†]

[†]The State Key Laboratory of Molecular Engineering of Polymers and Department of Macromolecular Science, Fudan University, Shanghai 200433, China

[‡]Shanghai Key Laboratory of Green Chemistry and Chemical Processes and School of Chemistry and Molecular Engineering, East China Normal University, Shanghai 200062, China

[§]Shanghai Pulmonary Hospital and School of Medicine, Tongji University, Shanghai 200433, China

[∥]Center for Soft Condensed Matter Physics and Interdisciplinary Research, School of Physical Science and Technology, Soochow University, Suzhou 215006, China

[⊥]School of Life Sciences, Fudan University, Shanghai 200433, China

[#]Department of Chemistry, University of South Florida, Tampa, Florida 33620, United States

[○]Shanghai Engineering Research Center of Molecular Therapeutics and New Drug Development, School of Chemistry and Molecular Engineering, East China Normal University, Shanghai 200062, China

Supporting Information

ABSTRACT: Bacterial biofilms are troublesome in the treatment of bacterial infectious diseases due to their inherent resistance to antibiotic therapy. Exploration of alternative antibiofilm reagents provides opportunities to achieve highly effective treatments. Herein, we propose a strategy to employ self-assembled saccharide-functionalized amphiphilic metallacycles ([**2+2**]-**Gal**, [**3+3**]-**Gal**, and [**6+6**]-**Gal**) with multiple positive charges as a different type of antibacterial reagent, marrying saccharide functionalization that interact with bacteria via "sweet talking". These self-assembled glyco-metallacycles gave various nanostructures (nanoparticles, vesicles or micron-sized vesicles) with different biofilms inhibition effect on *Staphylococcus aureus* (*S. aureus*). Especially, the peculiar self-assembly mechanism, superior antibacterial effect and biofilms inhibition distinguished the [**6+6**]-**Gal** from other metallacycles. Meanwhile, in vivo *S. aureus* pneumonia animal model experiments suggested that [**6+6**]-**Gal** could relieve mice pneumonia aroused by *S. aureus* effectively. In addition, the control study of metallacycle [**3+3**]-$\mathbf{EG_5}$ confirmed the significant role of galactoside both in the self-assembly process and the antibacterial efficacy. In view of the superior effect against bacteria, the saccharide-functionalized metallacycle could be a promising candidate as biofilms inhibitor or treatment agent for pneumonia.

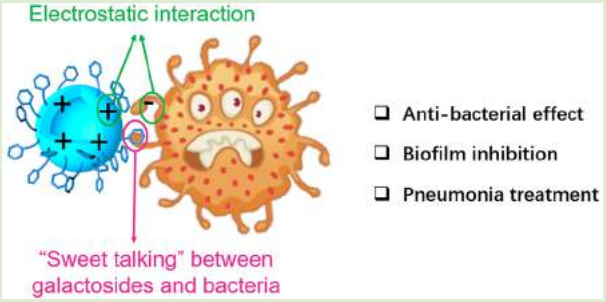

Biofilms are "aggregates of micro-organism" in which cells are encapsulated with large amounts of self-excreted inclusion, that is, extracellular polymeric substances (EPS), including polysaccharides, proteins, lipids, and DNA.[1] Because of the prevalence of biofilms, human infectious diseases caused by antibiotic-resistance bacteria cannot be effectively treated.[2] For example, infections associated with *S. aureus*, including osteomyelitis, periodontitis, chronic rhinosinusitis, chronic wound infection, and so on, resulted in more deaths and medical costs of typical hospitalizations.[3] In view of such threats, there are great demands for the design and development of biofilm inhibitors for efficient therapy of biofilm-caused diseases. Although many reagents in inhibition and elimination of *S. aureus* biofilms have been reported, for example, small molecules,[4] antimicrobial peptides,[5] surfactant-like molecules,[6] polymers,[7] and so on, it is still a challenging task to develop efficient and simple therapy.

Bacteria are covered with a heavy layer of polysaccharides.[8] Due to their abundance and structural diversity, these carbohydrates play crucial roles in biological functions,[9] especially mediating the communication between bacteria.[10] Thus, it is rational to design artificial materials covered with saccharides mimicking such saccharide-covered surfaces to interact with bacteria, as "camouflage" to the inside antibiofilm

Received: November 20, 2019
Accepted: December 23, 2019

DOI: 10.1021/acsmacrolett.9b00914
ACS Macro Lett. 2020, 9, 61−69

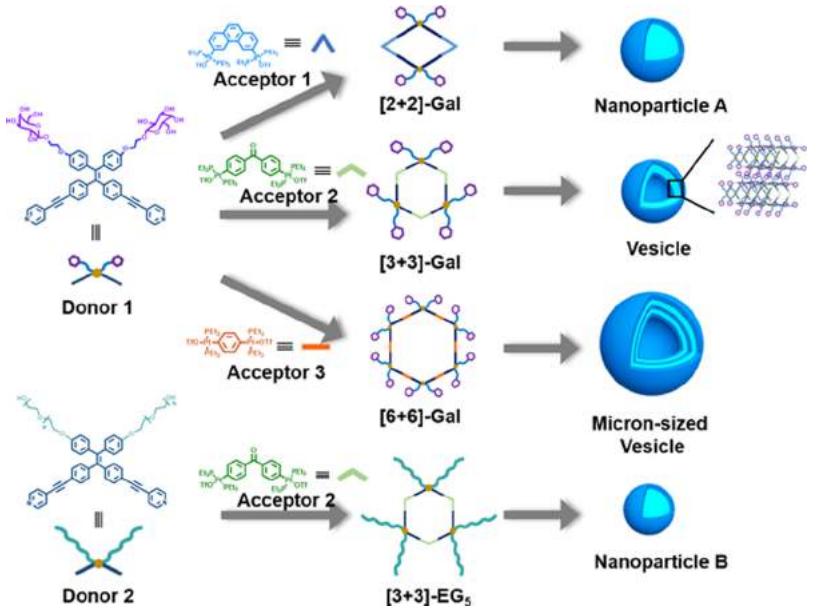

Figure 1. Schematic representation of the formation and hierarchical self-assembly morphologies of amphiphilic metallacycles.

reagent. Although glyco-containing materials have been employed as biofilms inhibitor in limited cases,[11] the interaction between the saccharides from materials and bacteria has been surprisingly overlooked.

In this work, a new strategy for biofilm inhibition assisted by artificial saccharide-coated assemblies to interact with bacteria via their "sweet-talking"[12] has been proposed. Inside the assemblies, organoplatinum(II) metallacycles were introduced as a precise and rigid scaffold providing multiple positive charges[13] for antibacteria and biofilms inhibition in a synergetic way. Herein, a series of glyco-metallacycles were designed and synthesized, which not only show attractive self-assembly behaviors, but also exhibit outstanding antibacterial and biofilms inhibition effect of *S. aureus* and could even alleviate the pneumonia of mice caused by *S. aureus* in vivo. It was found that the interaction between the assemblies and *S. aureus* is crucial for the antibacterial effect. To the best of our knowledge, this is the first report on bacterial and biofilms inhibition effect of hierarchical self-assembly of metallacycles, which demonstrates the orchestra of metallacycles and saccharides.

Donor 1 and **Donor 2** were synthesized through the esterification of tetraphenylethylene (TPE) moiety with bromine-substituted galactoside (Gal) or pentaethylene glycol (EG_5). These metallacycles were fabricated by blending donor and acceptor in a 1:1 ratio in methanol at room temperature through coordination-driven self-assembly (Figure 1). A series of spectroscopic techniques were used to confirm the formation of the desired metallacycles. All metallacycles showed sharp singlets with concomitant ^{195}Pt satellites corresponding to a single phosphorus environment revealed by the ^{31}P NMR spectra (Figure S1). These peaks in metallacycles shifted upfield from those of the corresponding starting di-Pt(II) acceptor. These changes, as well as the decrease in coupling of the flanking ^{195}Pt satellites, are consistent with the electron back-donation from the platinum atoms. The ^{1}H NMR spectra displayed significant downfield shifts of pyridyl proton signals on account of the loss of electron density upon coordination of the nitrogen atom with platinum atom (Figure S2). The sharp signals in both the ^{31}P and ^{1}H NMR spectra as well as the good solubility of these products implied the formation of discrete, highly symmetric species. Moreover, the assigned peaks in electrospray ionization time-of-flight mass spectrometry (ESI-TOF-MS) were isotopically resolved and in good agreement with their calculated theoretical distribution, which further confirmed the structure of metallacycles (Figure S3). Molecular simulation results by PM6 semiempirical molecular orbital method showed that each hexagonal metallacycle ([**3+3**]-**Gal**, [**6+6**]-**Gal**, and [**3+3**]-**EG_5**) featured a similar geometry with a hexagonal ring at the core surrounded by the outside hydrophilic moiety (Gal or EG_5) and [**2+2**]-**Gal** with a roughly planar rhomboid shape (Figure S4). Meanwhile, the saccharide-functionalized metallacycles displayed typical aggregation-induced emission (AIE) properties with the maximum emission wavelength at approximately 590 nm (Figures 2i and S5), which are distinctive with the previously reported TPE-based metallacycles that have a maximum emission wavelength at approximately 490 and 500 nm.[14] Interestingly, saccharide-functionalized metallacycles also presented different fluorescence emission wavelength from **Donor 1** (emission wavelength at 545 nm, Figure S5) and [**3+3**]-**EG_5** (emission wavelength at 550 nm, Figure S5), which means both the limited rotation by the metal-coordination bonds and different hydrophilic moiety could lead to the distinguished fluorescence properties in these amphiphilic metallacycles.

With the four kinds of metallacycles in hand, the metallacycles were first dissolved into methanol solvent, followed by dropping moderate water into the solution to prepare the glyco-assemblies (the final concentration of metallacycles is 5.0 mg/mL, see Supporting Information for details). After methanol volatilization, the obtained assemblies were characterized. Transmission electron microscopy (TEM) images showed that different metallacycles formed disparate morphologies (Figure 2a–d). Nanoparticles (NPs) were found for both [**2+2**]-**Gal** (Figure 2a) and [**3+3**]-**EG_5** (Figure 2d), while the obvious contrast between the interior and wall of the

DOI: 10.1021/acsmacrolett.9b00914
ACS Macro Lett. 2020, 9, 61−69

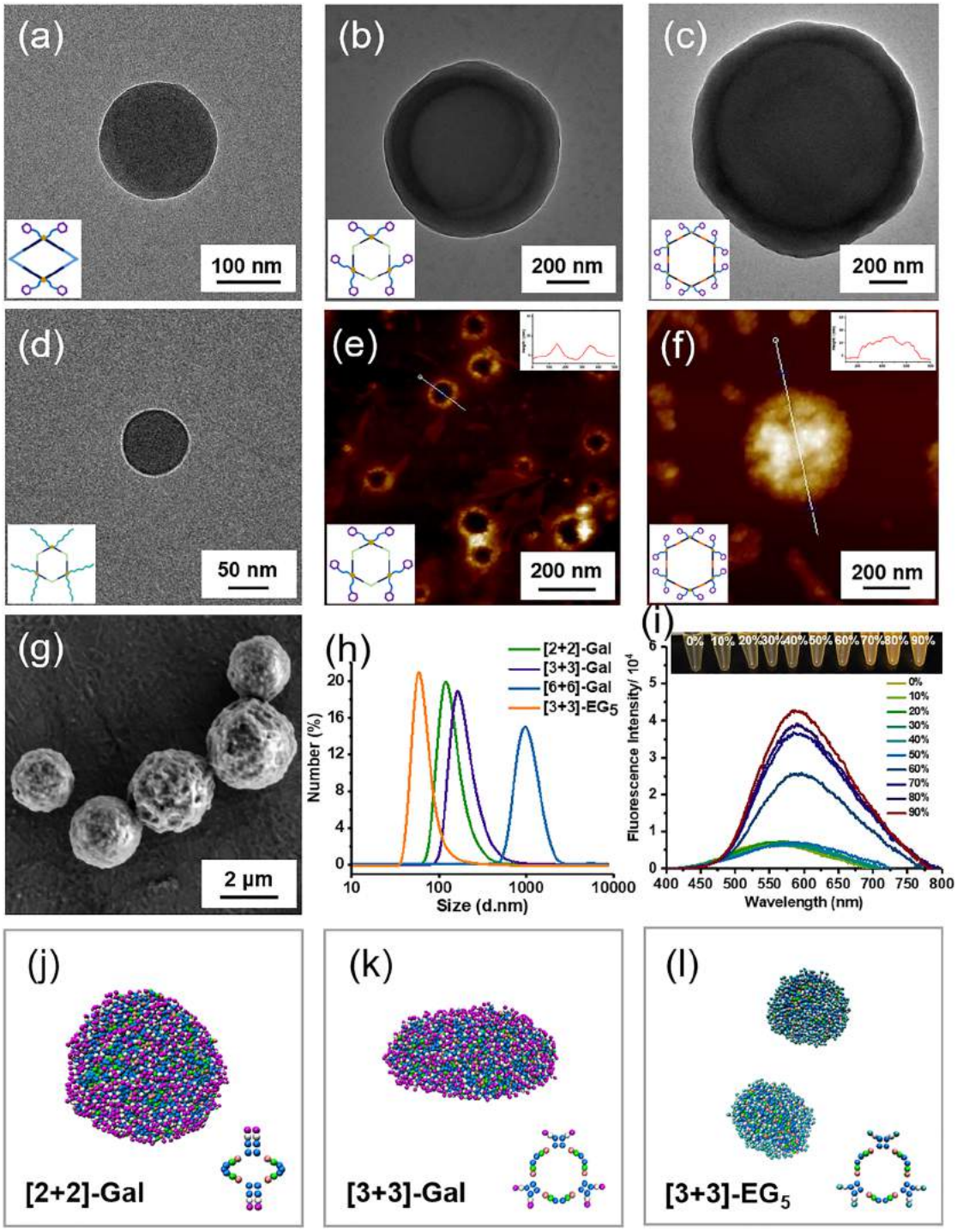

Figure 2. TEM images of (a) [**2+2**]-**Gal**, (b) [**3+3**]-**Gal**, (c) [**6+6**]-**Gal**, and (d) [**3+3**]-**EG$_5$** self-assemblies; AFM images of (e) [**3+3**]-**Gal**, (f) [**6+6**]-**Gal**; (g) SEM image of [**6+6**]-**Gal**; (h) DLS profile of self-assemblies; (i) Fluorescence emission spectrum of [**3+3**]-**Gal** metallacycle vs the H_2O fraction in the CH_3OH/H_2O mixtures (λ_{ex} = 330 nm, c = 0.5 mg/mL; inset: the photographs of [**3+3**]-**Gal** metallacycle in CH_3OH/H_2O mixtures with different fractions of H_2O on excitation at 365 nm using an ultraviolet lamp at 298 K (c = 0.5 mg/mL)); Snapshots of the assembly of (j) [**2+2**]-**Gal**, (k) [**3+3**]-**Gal**, and (l) [**3+3**]-**EG$_5$** during DPD simulations.

particles suggested the vesicle structure of [**3+3**]-**Gal** (Figure 2b) and micron-sized vesicle of [**6+6**]-**Gal** (Figure 2c). The average hydrodynamic diameters from dynamic light scattering (DLS) profile (Figure 2h) were in accordance with those observed size from the TEM images (ca. 145 nm for [**2+2**]-**Gal** NPs, 210 nm for [**3+3**]-**Gal** vesicles, ca. 1.08 μm for [**6+6**]-**Gal** micron-sized vesicles, and 72 nm for [**3+3**]-**EG$_5$** NPs). Atomic force microscopy (AFM), scanning electron microscope (SEM), and TEM energy-dispersive X-ray mapping results were in good agreement with TEM and DLS results (Figures 2 and S6−S9).

To understand these different nanostructures formed by the different amphiphilic metallacycles, dissipative particle dynamics (DPD) simulations (see details in Supporting Information) were employed to investigate the self-assembly mechanism at the molecular level. The modeling of metallacycles was

DOI: 10.1021/acsmacrolett.9b00914
ACS Macro Lett. 2020, 9, 61−69

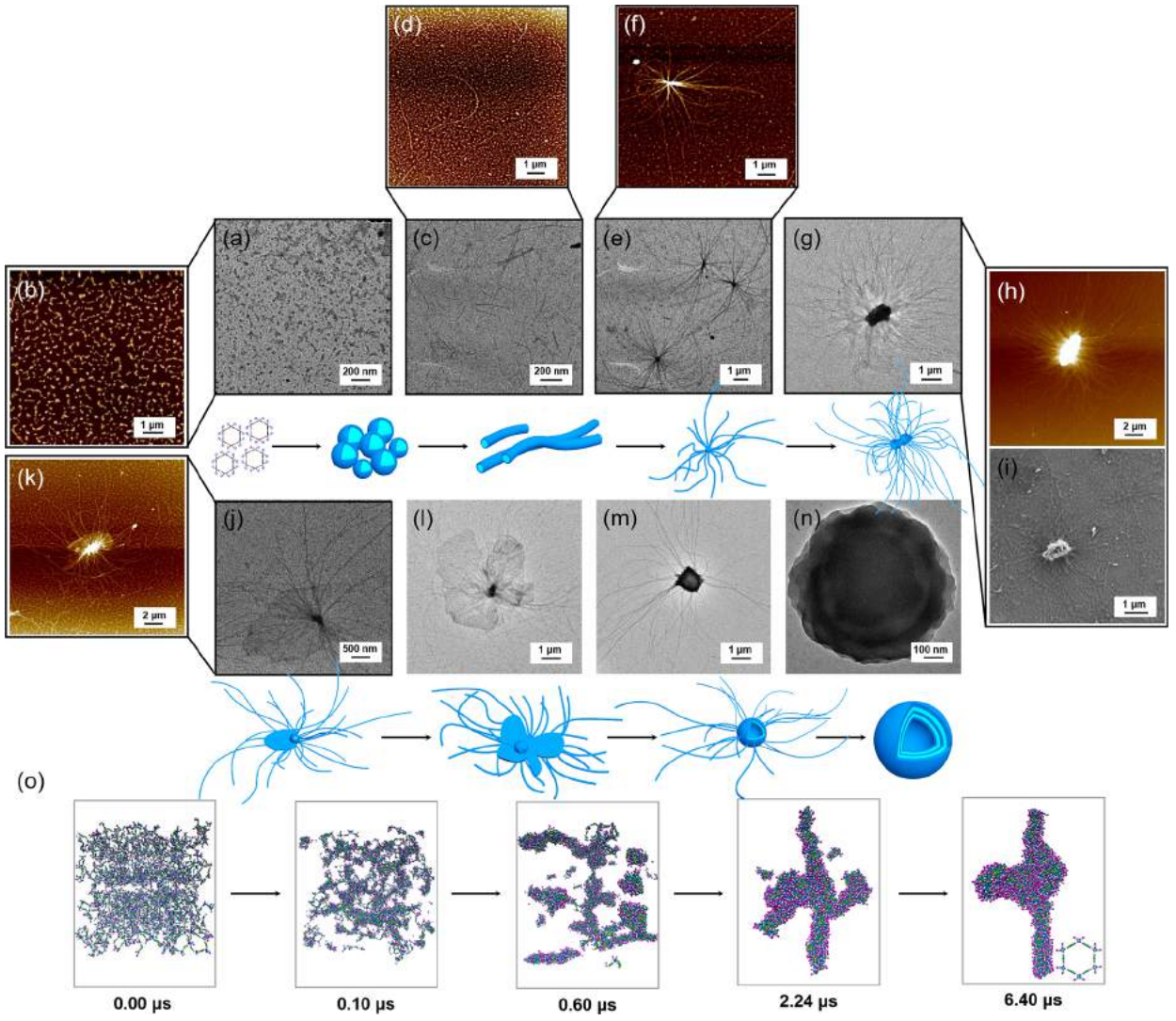

Figure 3. (a–n) TEM, AFM, and SEM images of the microsized vesicles by the self-assembly of [**6+6**]-**Gal** and proposed self-assembly mechanism; (o) Time sequence of snapshots illustrating the self-assembly process of [**6+6**]-**Gal** in the simulation.

established by using the coarse-grained (CG) method, where each group in the metallacycles was represented by using one CG bead (see the inset of Figures 2j–l and 3o). For [**2+2**]-**Gal**, about 300 metallacycle molecules were randomly placed in solvated box at the beginning of the simulation (Figure S14a). Due to the hydrophobicity of the metallacycle scaffold, the molecules quickly formed into small aggregates, and the size of the aggregates increased as standing time went on. Then these aggregates further fused with each other due to the $\pi-\pi$ stacking (i.e., effectively attractive interaction between aromatic beads). The carbohydrate–carbohydrate interactions (CCIs) resulting from the hydrogen bonds between hydroxyl groups and the hydrophobicity interaction among the ring of galactosides[15] also contribute to the further fusion of these aggregates. Finally, [**2+2**]-**Gal** assembled into NPs in the simulation (Figure 2j), which agreed well with the experimental findings. However, for [**3+3**]-**Gal**, because of the stronger CCIs resulted from the existence of more galactosides compared with [**2+2**]-**Gal**, these aggregates therefore further fused with each other and a piece of planar membrane occurred (Figures 2k and S14b). Finally, the layered structure can be observed, which may give some hints for the vesicle structures observed in the experiment. On the other hand, since the far weaker interaction among EG_5 molecules than CCIs, we did not consider the effective interaction between EG_5 beads in the simulations. As shown in Figures 2l and S13c, the [**3+3**]-**EG_5** molecules first formed aggregates, which was similar to the case of [**3+3**]-**Gal**. However, as standing time went on, due to the lack of CCIs, these aggregates did not change into the layered structure and the sphere NPs remained, which was in good agreement with the experimental results. Collectively, the balance between hydrophobicity and $\pi-\pi$ stacking of the metallacycles scaffold and the CCIs of galactosides contributes to the above special self-assembly behaviors, and the simulation results confirmed the importance of CCIs in the late stage of the self-assembly evolution process, demonstrating the significant impact of carbohydrates on the assembly morphology.

Compared with [**3+3**]-**Gal** hexagonal metallacycle, [**6+6**]-**Gal** that possesses more galactosides with a larger molecular size (Figure S4) may result in distinctive self-assembly behavior. Unexpectedly, [**6+6**]-**Gal** self-assembled into some micron-sized vesicles. TEM, AFM, and SEM were used to track the self-assembly process and the evolution profile of the morphologies has been depicted in Figure 3. Some small micelles were observed from TEM and AFM images initially

DOI: 10.1021/acsmacrolett.9b00914
ACS Macro Lett. 2020, 9, 61–69

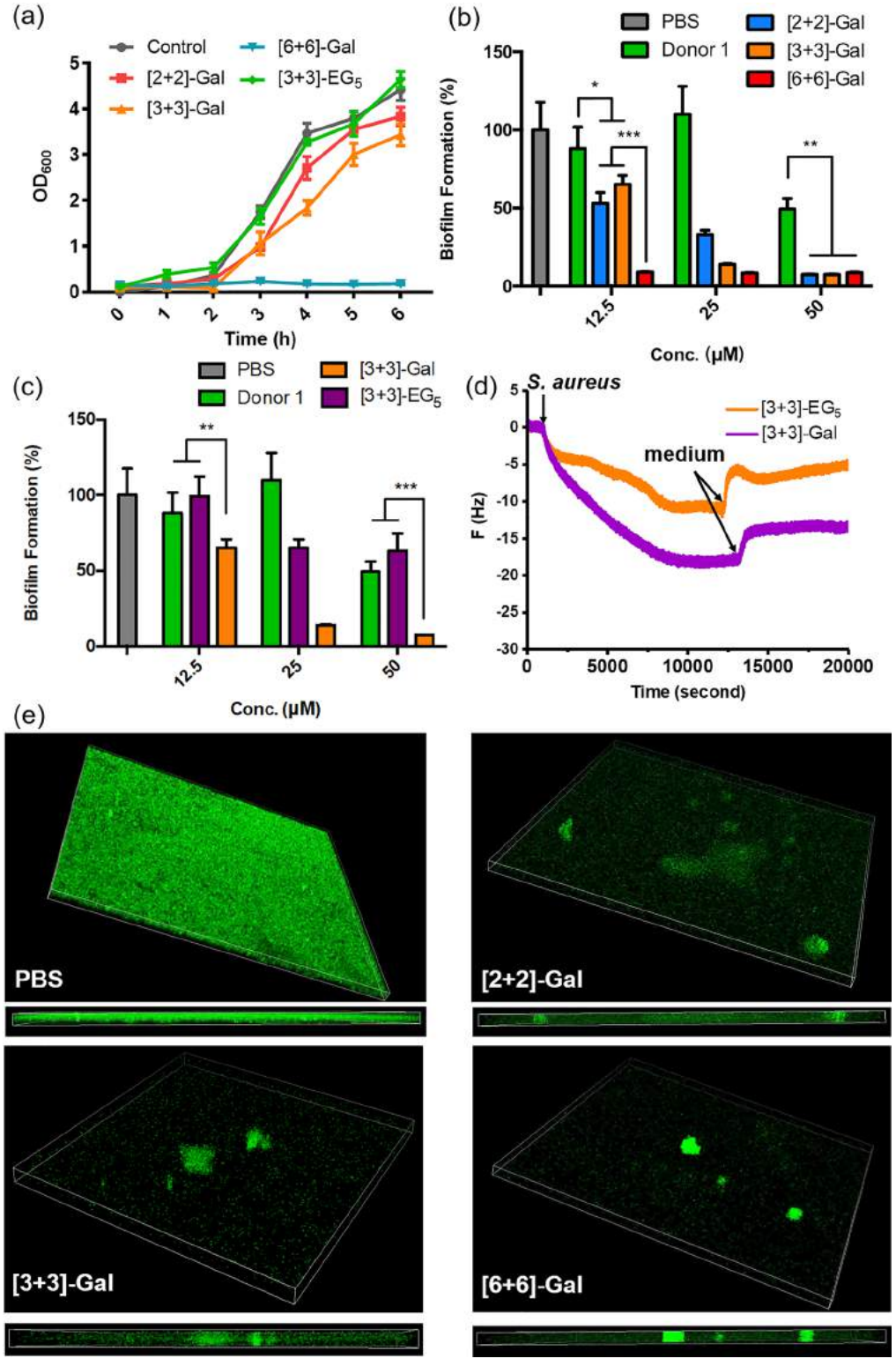

Figure 4. (a) Growth curves of *S. aureus* incubated with different metallacycle assemblies; Biofilms formation with different (b) glyco-metallacycle assemblies and (c) different [3 + 3] metallacycle assemblies; (d) Frequency response curves of the [**3+3**]-**Gal** and [**3+3**]-**EG$_5$** surface with *S. aureus* medium solution; (e) CLSM images of *S. aureus* biofilms after treatment with PBS, [**2+2**]-**Gal**, [**3+3**]-**Gal**, and [**6+6**]-**Gal** metallacycle assemblies. The concentrations of saccharide-functionalized metallacycles were all 2 mg/mL. Green fluorescence: the EPS stained by FITC-Con A; $*p < 0.05$, $**p < 0.01$, $***p < 0.001$.

(Figure 3a,b). Individual fibers fused by the small micelles at the early stage were observed, as shown in Figure 3c,d. Attractively, with standing time extended, the entanglement of fibers enabled the formation of some octopus-like particles (Figure 3e,f). Importantly, as shown in Figure 3g–i, it was found that the core of the octopus-like particles could grow (even micron-scale) with more fibers entangled with the core. In the adjacent regions to core, fibers showed the tendency to

DOI: 10.1021/acsmacrolett.9b00914
ACS Macro Lett. 2020, 9, 61−69

fuse together. Furthermore, the membrane structures were found (Figure 3j,k), which might be caused by the further fiber fusion. On the other hand, some fibers could still be discovered near the octopus-like particles confirming the fiber-fusion process. We proposed that the fusion tendency of fibers was resulted from their hydrophobic areas of relatively large metallacycle scaffold and the strong CCIs between [**6+6**]-**Gal**, even microsized membrane could be formed with further fusion (Figures 3l and S12). Thus, the membrane curved into vesicle-like structure with cavity (Figure 3m), and the micron-sized multiwall vesicles formed finally (Figure 3n). The evolution profile of the morphologies has been depicted in Figure 3. All the structures were also confirmed through AFM (Figure S10) and SEM (Figure S11) images.

Although the electronic microscopes could not follow the whole details of the self-assembly process of [**6+6**]-**Gal**, some important intermediate morphologies were also detected (Figure S12). DPD simulation could also provide some evidence for the morphology transition as observed in the experiment. As shown in Figure 3o, at the beginning (0.10 μs), due to the large size of metallacycle and multiple interacting sites in [**6+6**]-**Gal**, the molecules formed cross-linked network. The network further shrank to fiber structure to avoid the undesired interactions between the hydrophobic parts and water. Owing to the enhanced CCIs, the fiber further packed, and finally, a piece of "irregular" membrane was formed.

To study the effect of metallacycle assemblies against the bacteria, the antibacterial activity of metallacycle assemblies was evaluated by the propagation of *S. aureus*. Briefly, *S. aureus* was coincubated with different metallacycle assemblies with the same concentration of metallacycles, and OD_{600} was recorded every hour to evaluate the growth of *S. aureus*. As shown in Figures 4a and S15, [**6+6**]-**Gal** vesicles exhibited superior antibacterial activity than the other metallacycles assemblies. Meanwhile, [**3+3**]-**Gal** vesicles and [**2+2**]-**Gal** NPs showed slightly better antibacterial activity than [**3+3**]-$\mathbf{EG_5}$ NPs, indicating that the galactosides moiety contributed better to antibacterial activity.

Encouraged by the antibacterial activity of metallacycles, the efficacy of metallacycles assemblies to disrupt bacterial biofilms was evaluated by crystal violet staining assay (see Supporting Information for details). Different concentrations of the metallacycle assemblies were coincubated with equivoluminal planktonic *S. aureus* for 24 h. Afterward, the biofilms of *S. aureus* were quantified by the absorbance of crystal violet at 590 nm (Table S1). The biofilm formation results (calculated according to the formula in Supporting Information) are shown in Figure 4b,c. The capacity in biofilms inhibition of different metallacycle assemblies and **Donor 1** was compared to investigate the role that metallacycle assemblies played in biofilm inhibition (Figure 4b). The three metallacycle assemblies demonstrated satisfactory biofilm inhibition activity at 25 μM concentration (consistent concentration of metallacycles), which is much better than the performance of **Donor 1**. Furthermore, even at a relatively low concentration (12.5 μM), [**6+6**]-**Gal** vesicles still showed over 90% inhibition, which is much better than those of [**2+2**]-**Gal** NPs and [**3+3**]-**Gal** vesicles on biofilms inhibition. To further demonstrate the contribution of galactosides, the biofilm inhibition properties of **Donor 1**, [**3+3**]-**Gal** vesicles, and [**3+3**]-$\mathbf{EG_5}$ NPs were investigated at the same concentration. Figure 4c revealed that [**3+3**]-**Gal** vesicles showed a strong biofilm inhibition effect, while [**3+3**]-$\mathbf{EG_5}$ NPs and **Donor 1** showed little biofilms inhibition effect. The difference was even much more significant at 50 μM, which suggested that galactosides played an important role in inhibition of biofilms of *S. aureus*. The biofilms experiments agreed well with the antibacterial effect in proliferation curves. As mentioned above, [**6+6**]-**Gal** vesicles exhibited a strong biofilm inhibition effect even at very low concentration, which surpassed the effect in many reported works.[7,16] Visualized evidence in biofilms inhibition has been provided by confocal laser scanning microscopy (CLSM) 3D images (Figure 4e). Biofilms were fixed with absolute ethyl alcohol and labeled with FITC-Concanavalin A, which labels EPS of biofilms.[17] The samples with an addition of [**2+2**]-**Gal** NPs, [**3+3**]-**Gal** vesicles, and [**6+6**]-**Gal** vesicles (2 mg/mL) showed nearly no biofilms formation.

The interaction between *S. aureus* and saccharide-functionalized metallacycles was investigated to gain further insight into the mechanism of biofilms inhibition. As shown in Figure S16, owing to the intrinsic fluorescence of metallacycles, 358 nm laser was used to excite without any other external dyes to stain, all *S. aureus* were observed in the bright field overlapped with metallacycle assemblies. This result demonstrated that the strong interaction between *S. aureus* and metallacycle assemblies. *S. aureus* possesses considerably negative charges because of external components (mainly proteins and lipids) of bacteria.[18] Therefore, zeta (ζ) potential was employed to investigate the interaction between metallacycle assemblies and *S. aureus* (Tables S2 and S3). The value of ζ potential increased from −27.7 to 33.2 V after 2.0 mg/mL [**3+3**]-**Gal** metallacycle assemblies was added, while [**3+3**]-$\mathbf{EG_5}$ showed similar result. The increase of ζ potential indicated the binding between *S. aureus* and metallacycle assemblies was through electrostatic interaction, but may not explain the reason for better biofilm inhibition performed by [**3+3**]-**Gal** than [**3+3**]-$\mathbf{EG_5}$. By using quartz crystal microbalance (QCM), the interaction between assemblies and *S. aureus* was further quantified (Figure 4d), where the metallacycle assemblies were immobilized on the surface of gold chip. The frequency decreased after *S. aureus* solution was loaded to the [**3+3**]-**Gal**-modified gold chip (purple curve in Figure 4d), indicating the successful absorption of bacteria on the surface. After the frequency reached equilibrium, medium was flowed onto the chip in order to remove any nonspecific interacting bacteria. Thus, the observed decrease in frequency (from 0 to −15 Hz) indicates the strong interaction between [**3+3**]-**Gal** and *S. aureus*. As a control, the decrease in frequency of [**3+3**]-$\mathbf{EG_5}$ modified gold chip after the similar treatment was negligible (from 0 to −5 Hz). It is known that the weight of gold chip increases accompanying with the frequency decrease.[19] The above difference of decrease in frequency suggested that the glyco-metallacycles assemblies interact with *S. aureus* more effectively through interaction ("sweet talking") between galactosides and *S. aureus*, which could not be achieved via EG_5 modification of [**3+3**]-$\mathbf{EG_5}$. In short, the QCM result indicated that galactoside involved in the association between saccharide-functionalized metallacycle assemblies and *S. aureus*. Hence, according to the antibacterial experiment, ζ potential, and QCM results, we concluded that electrostatic interaction contributes little to the biofilm inhibition since [**3+3**]-$\mathbf{EG_5}$, with strong electrostatic interaction exhibiting weak biofilm inhibition. More importantly, the "sweet talking" between galactosides and *S. aureus* gave great contribution to biofilm inhibition ([**3+3**]-**Gal** with higher biofilm inhibition than [**3+3**]-$\mathbf{EG_5}$).

DOI: 10.1021/acsmacrolett.9b00914
ACS Macro Lett. 2020, 9, 61−69

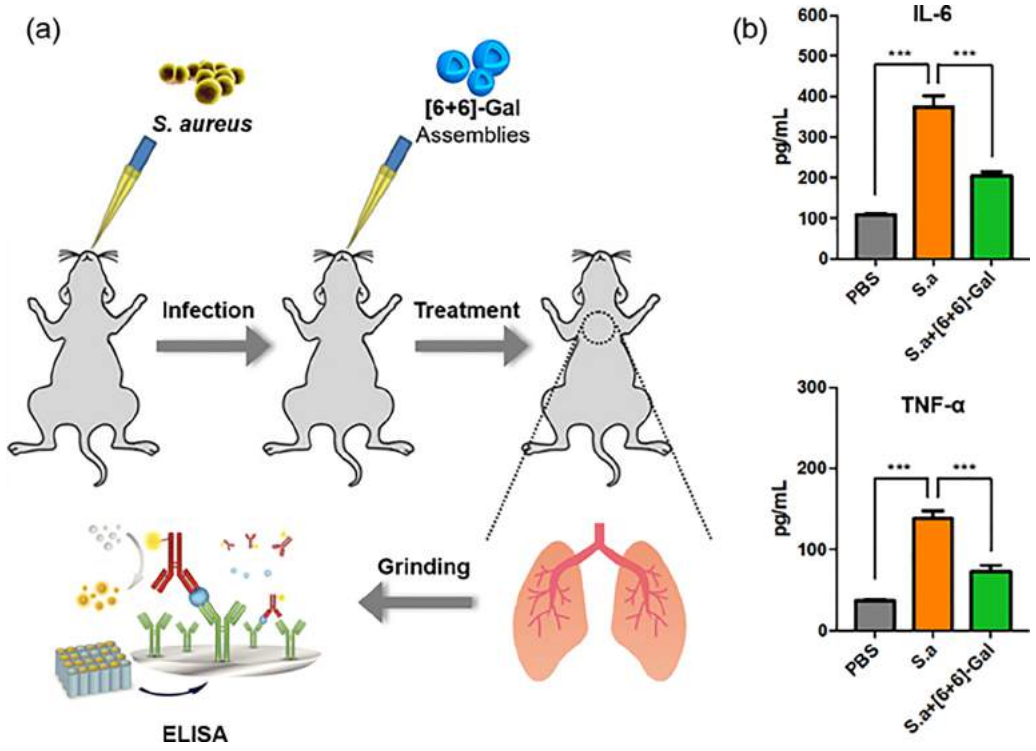

Figure 5. (a) Scheme of *S. aureus* penumonia animal model to assess the effect of [**6+6**]-**Gal** assemblies on alleviating pneumonia, (b) IL-6, THF-α was detected by ELISA to indicate the inhibition of inflammatory effect of *S. aureus*; ***$p < 0.001$.

S. aureus is the most common purulent infectious pathogen in humans. When *S. aureus* infects the body, it might cause some fatal diseases including pericarditis, pneumonia, sepsis, and so on.[20] Clinical data[21] showed that *S. aureus* pneumonia was already widespread worldwide with a high mortality rate, which poses a great challenge to human health. As a proof-of-concept demonstration of the potential of pneumonia inhibitor, herein, *S. aureus* pneumonia animal model was established to test whether saccharide-functionalized metallacycles assemblies can resist against lung disease. As shown in Figure 5a, after establishing the model of acute pulmonary *S. aureus* (2×10^9 cfu/mL) infection, mice were added by intratracheally instilling exogenously PBS or [**6+6**]-**Gal** vesicles (35 μL, 10 μM). A total of 24 h later, the lung tissue was ground and the lung homogenates were used to measure the secretion of IL-6 and TNF-α since these two kinds of cytokines could reflect the inflammation level. Figure 5b showed that cytokines of the *S. aureus* group are higher than that of PBS control group, indicating the successful establishment of *S. aureus* pneumonia model. Meanwhile, the cytokines of the group with [**6+6**]-**Gal** assemblies showed obvious decrease compared with that of *S. aureus* group. The decrease of the value of IL-6 and TNF-α demonstrated the high efficiency of [**6+6**]-**Gal** assemblies in alleviating pneumonia in mice. This enzyme-linked immunosorbent assay (ELISA) experiment suggested that [**6+6**]-**Gal** assemblies could be used as the potential pneumonia treatment reagent effectively.

In summary, a series of amphiphilic saccharide-functionalized metallacycles were constructed and these metallacycles displayed special self-assembly behaviors with different morphologies (nanoparticles, vesicles, octopus-like particles and micron-sized vesicles). Evolution profile of the morphologies and molecular simulation method were utilized to further shed light on the mechanism of self-assembly. Significantly, [**6+6**]-**Gal** exhibited excellent biofilms inhibition of *S. aureus*, even at a very low concentration, owing to the synergistic effect of electrostatic interaction between metallacycle assemblies and *S. aureus* as well as the interaction ("sweet talking") between galactoside and *S. aureus*. Furthermore, [**6+6**]-**Gal** vesicles can effectively relieve pneumonia of mice caused by *S. aureus*. This work opens a new avenue on biofilm inhibitor design based on the interaction between the saccharides from the inhibitor and the bacteria.

■ ASSOCIATED CONTENT

Supporting Information

The Supporting Information is available free of charge at https://pubs.acs.org/doi/10.1021/acsmacrolett.9b00914.

Experimental methods, synthetic procedures, and the characterization of compounds and metallacycles, electronic microscope characterization, computational dynamic simulation for self-assembly behaviors of metallacycles, and the antibacterial experiment (PDF)

■ AUTHOR INFORMATION

Corresponding Authors

*E-mail: guosong@fudan.edu.cn.
*E-mail: hbyang@chem.ececnu.edu.cn.
*E-mail: jfxucn@163.com.

ORCID

Xiaojuan Liao: 0000-0002-6046-8831
Xiaopeng Li: 0000-0001-9655-9551
Hong-ming Ding: 0000-0002-9224-4779
Hai-Bo Yang: 0000-0003-4926-1618
Guosong Chen: 0000-0001-7089-911X

DOI: 10.1021/acsmacrolett.9b00914
ACS Macro Lett. 2020, 9, 61−69

Notes

The authors declare no competing financial interest.

■ ACKNOWLEDGMENTS

G.C. thanks NSFC/China (Nos. 51721002, 21861132012, and 91527305). H.-B.Y. acknowledges NSFC/China (No. 21625202), STCSM (No. 16XD1401000), and the Program for Changjiang Scholars and Innovative Research Team in University for financial support.

■ REFERENCES

(1) (a) Flemming, H. C.; Wingender, J. The biofilm matrix. *Nat. Rev. Microbiol.* **2010**, *8*, 623−633. (b) Flemming, H. C.; Wingender, J.; Szewzyk, U.; Steinberg, P.; Rice, S. A.; Kjelleberg, S. Biofilms: an emergent form of bacterial life. *Nat. Rev. Microbiol.* **2016**, *14*, 563−575.

(2) (a) Bridier, A.; Briandet, R.; Thomas, V.; Dubois-Brissonnet, F. Resistance of bacterial biofilms to disinfectants: a review. *Biofouling* **2011**, *27*, 1017−103227. (b) Hoiby, N.; Bjarnsholt, T.; Givskov, M.; Molin, S.; Ciofu, O. Antibiotic resistance of bacterial biofilms. *Int. J. Antimicrob. Agents* **2010**, *35*, 322−332.

(3) (a) Wenzel, R. P.; Edmond, M. B. The impact of hospital-acquired bloodstream infections. *Emerging Infect. Dis.* **2001**, *7*, 174−177. (b) Hall-Stoodley, L.; Costerton, J. W.; Stoodley, P. Bacterial biofilms: from the natural environment to infectious diseases. *Nat. Rev. Microbiol.* **2004**, *2*, 95−108. (c) Archer, N. K.; Mazaitis, M. J.; Costerton, J. W.; Leid, J. G.; Powers, M. E.; Shirtliff, M. E. Staphylococcus aureus biofilms. *Virulence* **2011**, *2*, 445−459.

(4) (a) Bottcher, T.; Kolodkin-Gal, I.; Kolter, R.; Losick, R.; Clardy, J. Synthesis and activity of biomimetic biofilm disruptors. *J. Am. Chem. Soc.* **2013**, *135*, 2927−2930. (b) Barraud, N.; Kardak, B. G.; Yepuri, N. R.; Howlin, R. P.; Webb, J. S.; Faust, S. N.; Kjelleberg, S.; Rice, S. A.; Kelso, M. J. Cephalosporin-3′-diazeniumdiolates: targeted NO-donor prodrugs for dispersing bacterial biofilms. *Angew. Chem., Int. Ed.* **2012**, *51*, 9057−9060.

(5) Kolodkin-Gal, I.; Romero, D.; Cao, S.; Clardy, J.; Kolter, R.; Losick, R. D-amino acids trigger biofilm disassembly. *Science* **2010**, *328*, 627−629.

(6) (a) Wang, R.; Khan, B. A.; Cheung, G. Y.; Bach, T. H.; Jameson-Lee, M.; Kong, K. F.; Queck, S. Y.; Otto, M. Staphylococcus epidermidis surfactant peptides promote biofilm maturation and dissemination of biofilm-associated infection in mice. *J. Clin. Invest.* **2011**, *121*, 238−248. (b) Percival, S. L.; Mayer, D.; Kirsner, R. S.; Schultz, G.; Weir, D.; Roy, S.; Alavi, A.; Romanelli, M. Surfactants: Role in biofilm management and cellular behaviour. *Int. Wound J.* **2019**, *16*, 753−760.

(7) (a) Li, J.; Zhang, K.; Ruan, L.; Chin, S. F.; Wickramasinghe, N.; Liu, H.; Ravikumar, V.; Ren, J.; Duan, H.; Yang, L.; Chan-Park, M. B. Block Copolymer Nanoparticles Remove Biofilms of Drug-Resistant Gram-Positive Bacteria by Nanoscale Bacterial Debridement. *Nano Lett.* **2018**, *18*, 4180−4187. (b) Zhang, P.; Li, S.; Chen, H.; Wang, X.; Liu, L.; Lv, F.; Wang, S. Biofilm Inhibition and Elimination Regulated by Cationic Conjugated Polymers. *ACS Appl. Mater. Interfaces* **2017**, *9*, 16933−16938.

(8) Schäffer, C.; Messner, P. The structure of secondary cell wall polymers: how Gram-positive bacteria stick their cell walls together. *Microbiology* **2005**, *151*, 643−651.

(9) (a) Pilobello, K. T.; Mahal, L. K. Deciphering the glycocode: the complexity and analytical challenge of glycomics. *Curr. Opin. Chem. Biol.* **2007**, *11*, 300. (b) Kiessling, L. L.; Cairo, C. W. Hitting the sweet spot. *Nat. Biotechnol.* **2002**, *20*, 234.

(10) Bertozzi, C. R.; Kiessling, L. L. Chemical Glycobiology. *Science* **2001**, *291*, 2357−2364.

(11) (a) Kadam, R. U.; Bergmann, M.; Hurley, M.; Garg, D.; Cacciarini, M.; Swiderska, M. A.; Nativi, C.; Sattler, M.; Smyth, A. R.; Williams, P.; Camara, M.; Stocker, A.; Darbre, T.; Reymond, J. L. A glycopeptide dendrimer inhibitor of the galactose-specific lectin LecA and of Pseudomonas aeruginosa biofilms. *Angew. Chem., Int. Ed.* **2011**, *50*, 10631−10635. (b) Sommer, R.; Wagner, S.; Rox, K.; Varrot, A.; Hauck, D.; Wamhoff, E. C.; Schreiber, J.; Ryckmans, T.; Brunner, T.; Rademacher, C.; Hartmann, R. W.; Bronstrup, M.; Imberty, A.; Titz, A. Glycomimetic, Orally Bioavailable LecB Inhibitors Block Biofilm Formation of Pseudomonas aeruginosa. *J. Am. Chem. Soc.* **2018**, *140*, 2537−2545.

(12) (a) Pasparakis, G.; Alexander, C. Sweet talking double hydrophilic block copolymer vesicles. *Angew. Chem., Int. Ed.* **2008**, *47*, 4847−4850. (b) Yu, G.; Ma, Y.; Han, C.; Yao, Y.; Tang, G.; Mao, Z.; Gao, C.; Huang, F. A sugar-functionalized amphiphilic pillar[5]-arene: synthesis, self-assembly in water, and application in bacterial cell agglutination. *J. Am. Chem. Soc.* **2013**, *135*, 10310−10313. (c) Wu, D.; Shen, J.; Bai, H.; Yu, G. Supramolecular self-assemblies for bacterial cell agglutination driven by directional charge-transfer interactions. *Chem. Commun.* **2018**, *54*, 2922−2925. (d) Lee, D. W.; Kim, T.; Park, I. S.; Huang, Z.; Lee, M. Multivalent nanofibers of a controlled length: regulation of bacterial cell agglutination. *J. Am. Chem. Soc.* **2012**, *134*, 14722−14725.

(13) (a) Datta, S.; Saha, M. L.; Stang, P. J. Hierarchical Assemblies of Supramolecular Coordination Complexes. *Acc. Chem. Res.* **2018**, *51*, 2047−2063. (b) Cook, T. R.; Stang, P. J. Recent Developments in the Preparation and Chemistry of Metallacycles and Metallacages via Coordination. *Chem. Rev.* **2015**, *115*, 7001−7045.

(14) (a) Yan, X.; Wang, M.; Cook, T. R.; Zhang, M.; Saha, M. L.; Zhou, Z.; Li, X.; Huang, F.; Stang, P. J. Light-Emitting Superstructures with Anion Effect: Coordination-Driven Self-Assembly of Pure Tetraphenylethylene Metallacycles and Metallacages. *J. Am. Chem. Soc.* **2016**, *138*, 4580−4588. (b) Tian, Y.; Yan, X.; Saha, M. L.; Niu, Z.; Stang, P. J. Hierarchical Self-Assembly of Responsive Organoplatinum(II) Metallacycle-TMV Complexes with Turn-On Fluorescence. *J. Am. Chem. Soc.* **2016**, *138*, 12033−12036. (c) Yan, X.; Wang, H.; Hauke, C. E.; Cook, T. R.; Wang, M.; Saha, M. L.; Zhou, Z.; Zhang, M.; Li, X.; Huang, F.; Stang, P. J. A Suite of Tetraphenylethylene-Based Discrete Organoplatinum(II) Metallacycles: Controllable Structure and Stoichiometry, Aggregation-Induced Emission, and Nitroaromatics Sensing. *J. Am. Chem. Soc.* **2015**, *137*, 15276−15286.

(15) de la Fuente, J. M.; Penades, S. Understanding carbohydrate-carbohydrate Interactions by means of glyconanotechnology. *Glycoconjugate J.* **2004**, *21*, 149−163. (b) Qi, W.; Zhang, Y.; Wang, J.; Tao, G.; Wu, L.; Kochovski, Z.; Gao, H.; Chen, G.; Jiang, M. Deprotection-Induced Morphology Transition and Immunoactivation of Glycovesicles: A Strategy of Smart Delivery Polymersomes. *J. Am. Chem. Soc.* **2018**, *140*, 8851−8857. (c) Su, L.; Wang, C.; Polzer, F.; Lu, Y.; Chen, G.; Jiang, M. Glyco-Inside Micelles and Vesicles Directed by Protection−Deprotection Chemistry. *ACS Macro Lett.* **2014**, *3*, 534−539.

(16) Liu, Y.; Busscher, H. J.; Zhao, B.; Li, Y.; Zhang, Z.; van der Mei, H. C.; Ren, Y.; Shi, L. Surface-Adaptive, Antimicrobially Loaded, Micellar Nanocarriers with Enhanced Penetration and Killing Efficiency in Staphylococcal Biofilms. *ACS Nano* **2016**, *10*, 4779−4789.

(17) (a) Vu, B.; Chen, M.; Crawford, R. J.; Ivanova, E. P. Bacterial extracellular polysaccharides involved in biofilm formation. *Molecules* **2009**, *14*, 2535−2554. (b) Azeredo, J.; Azevedo, N. F.; Briandet, R.; Cerca, N.; Coenye, T.; Costa, A. R.; Desvaux, M.; Di Bonaventura, G.; Hebraud, M.; Jaglic, Z.; Kacaniova, M.; Knochel, S.; Lourenco, A.; Mergulhao, F.; Meyer, R. L.; Nychas, G.; Simoes, M.; Tresse, O.; Sternberg, C. Critical review on biofilm methods. *Crit. Rev. Microbiol.* **2017**, *43*, 313−351.

(18) Sonohara, R.; Muramatsu, N.; Ohshima, H.; Kondo, T. Difference in surface properties between Escherichia coli and Staphylococcus aureus as revealed by electrophoretic mobility measurements. *Biophys. Chem.* **1995**, *55*, 273−277.

(19) Rodahl, M.; Hook, F.; Fredriksson, C.; Keller, C. A.; Krozer, A.; Brzezinski, P.; Voinova, M.; Kasemo, B. Simultaneous Frequency and Dissipation Factor QCM Measurements of Biomolecular Adsorption and Cell Adhesion. *Faraday Discuss.* **1997**, *107*, 229−246.

DOI: 10.1021/acsmacrolett.9b00914
ACS Macro Lett. 2020, 9, 61−69

(20) (a) Archer, N. K.; Mazaitis, M. J.; Costerton, J. W.; Leid, J. G.; Powers, M. E.; Shirtliff, M. E. Staphylococcus aureus biofilms: properties, regulation, and roles in human disease. *Virulence* **2011**, *2*, 445−459. (b) Otto, M. Staphylococcal biofilms. *Curr. Top. Microbiol. Immunol.* **2008**, *322*, 207−228.

(21) (a) Klevens, R. M.; Morrison, M. A.; Nadle, J.; Petit, S.; Gershman, K.; Ray, S.; Harrison, L. H.; Lynfield, R.; Dumyati, G.; Townes, J. M.; Craig, A. S.; Zell, E. R.; Fosheim, G. E.; McDougal, L. K.; Carey, R. B.; Fridkin, S. K. Invasive Methicillin-Resistant Staphylococcus aureus Infections in the United States. *JAMA* **2007**, *298*, 1763−1771. (b) Kuehnert, M. J.; Hill, H. A.; Kupronis, B. A.; Tokars, J. I.; Solomon, S. L.; Jernigan, D. B. Methicillin-resistant−Staphylococcus aureus Hospitalizations, United States. *Emerging Infect. Dis.* **2005**, *11*, 868−872.

DOI: 10.1021/acsmacrolett.9b00914
ACS Macro Lett. 2020, 9, 61−69